Hydrodynamics of a dual-module pontoon-net floating breakwater system: numerical simulations and prototype tests

Yong Cheng[a], Chunyan Ji[a*], Xuekang Gu[b], Fali Huo[a], Jie Cui[a], Zhi-Ming Yuan[a, c]

[a]*School of naval architecture and ocean engineering, Jiangsu University of Science and Technology, Zhenjiang, 212003, China*

[b]*China ship scientific research center, Wuxi, 213082, China*

[c]*Department of Naval Architecture, Ocean and Marine Engineering, University of Strathclyde, Glasgow, G4 0LZ, UK*

ABSTRACT

Floating breakwaters (FBs) with a mooring system have been widely applied to protect marine infrastructures (e.g. artificial beach or island, aquaculture farm or marine vessels in harbors) from being destroyed by ocean waves. In this paper, an innovative cylindrical dual pontoon-net FB was developed to enhance the wave attenuation capacity of the FB, and then this dual-module FB system was constructed as the prototype for on-site testing. A fully nonlinear time-domain model based on a coupled iterative solution of water integral equation, floating body and net dynamic equations, was proposed to simulate the interaction of waves and the FB system. The flow field around the nets was simulated by introducing a porous-media model with Darcy's law, while the deformation of the flexible nets was solved by using the lumped mass model. The instantaneous free surface was captured using the mixed Eulerian-Lagrangian (MEL) approach which employs an improved moving-grid technique based on the spring analysis to remesh the instantaneous water surface and wetted body surface. Also, on-site tests were conducted to evaluate wave transmission performance of the FB system and to validate the numerical model. The comparisons indicated that the numerical solution was in good agreement with the measured data. Then, the effects of incident wave direction, wave period, wave height, net height, net number and net porosity on the hydrodynamic performance of the FB system were emphatically examined.

Keywords: Floating breakwater, fully nonlinear simulations, on-site tests, flexible net, wave attenuation, moving-grid technique

1. Introduction

Net cages can be used as an effective fish-farming platform system for allowing the passage of currents, exchanging water, and protecting the health and growth of fish. On the other hand, dual-pontoon floating breakwater (DPFB) has been considered as an eco-friendly breakwater as they attenuate surface waves in the same way as single pontoon floating breakwaters (SPFBs), but in addition reduce the wave field through wave resonance in the gap between two single pontoons. The proposed DPFB for port engineering and marine aquaculture consists of a cylindrical dual-pontoon with one or more vertical rows of nets underneath. When waves propagate toward the floating breakwater, the incident wave energy can be altered due to wave resonance, generation of turbulence, motion of structure and net damping effect. Therefore, the investigation on the hydrodynamic performance of the innovative floating breakwater has become an important subject.

Numerical wave tank (NWT) which has been developed as an effective and efficient tool for

* Corresponding author. Chunyan Ji, doctor, mainly research in wave action on maritime structure, E-mail: jichunyanjkd@163.com

This is a peer reviewed, accepted author manuscript of the following research article: Cheng, Y., Ji, C., Gu, X., Huo, F., Cui, J., & Yuan, Z-M. (2021). Hydrodynamics of a dual-module pontoon-net floating breakwater system : numerical simulations and prototype tests. Journal of Hydrodynamics, 33, 915–927. https://doi.org/10.1007/s42241-021-0081-1

modeling the interaction of waves and floating structures, can be generally categorized into two groups: potential-flow models and viscous-flow models based on the Navier-Stokes equations solver. The potential-flow models are derived by simplifying the Navier-Stokes (N-S) equations ignoring fluid viscous effect, and are discretised by constant and higher order boundary element method (BEM). This enables the solutions in a affordable time on standard computers, although the models are usually restricted to non-breaking waves and wave problems up to the breaking point, as described by Zang et al. (2006). In recent years, some researchers have developed the fully nonlinear BEM-based NWTs to solve wave-structure interaction problems, like Koo and Kim (2004), Koo and Kim (2007), Tang et al. (2011), Ning et al. (2015) and Cheng et al. (2017), who use the mixed Eulerian-Lagrangian (MEL) technique to update the time-dependent free surface with moving nodes. The viscous models have the potential to provide better solutions for high non-linear phenomena such as flow separation, wave breaking and overtopping, despite demanding a higher computational cost. Pham (2005) simulated wave-structure interaction by using Computational Fluid Dynamics (CFD). He applied a combination of dam-break model and water jet model for handling extremely nonlinear phenomena such as green water impinging on the fixed deck of an advancing ship in waves. Westphalen et al. (2012) investigated the flow field around a fixed horizontal and vertical cylinders using N-S equations and Finite volume method (FVM), however, the motions of the floating structure were not considered in their works. The viscous models faced a difficulty of the treatment of the varying positions of the floating body during each cycle of movement under the wave action. Therefore, the updating of grid system around the moving boundary of a floating structure is essential in numerical simulations. A body-fitted mesh to body motion had been accomplished with grid deformation, overset grid or grid regeneration by many researchers. For example, Mittal and kumar (2001) set a part of the grid around the floating structure, with moving the part together with structure, and keeping the outer part fixed. In this case, the outer domain was not affected by the body motion and the meshes around the body kept a good quality, but the method was limited to single-degree-freedom motion by adjusting the nodes at boundaries of the solution domain. In order overcome this difficulty, Hadzic et al. (2005) employed multiblock structural grids with a combination of mesh motion, mesh deformation and sliding mesh interfaces, to model flow-induced body motion in large irregular waves, including a free-fall drop of an open container into water. Simonsen et al. (2013) adopted overset multiblock chimera grids to model the heave and pitch motions of the ship in regular head waves and validated their CFD solutions by conducting a series of relevant model tests. Sadat-Hosseini et al. (2013) extended the technique to develop 3D overset, multiblock structural grids for predicting the added resistance and motions of ship. However, the grid interpolation between overset grids for moving structure requires considerable time and effort. Chen et al. (2017) divided re-gridding region around the floating structure using unstructured mesh. This can be applicable to arbitrary body motions but often leads to excessive distortion of meshes in a fierce motion.

To better simulate the flow field around the net cage, extensive research has been performed in the past decades, whilst studies of the flexibility and movement of the net are rare. Fredriksson (2001) carried out a series of experiments to measure the flow velocity in an open ocean cage, and an approximate 10% velocity reduction was found. Johansson et al. (2007) measured the current velocity around the net cages at four farms in Norway, and found a current reduction between 33% and 64%. Zhao et al. (2013) treated the net cage as a porous medium, and investigated the effect of the plane net parameter such as inclination angles, net heights and net numbers on flow field. Later,

Bi et al. (2014) further considered the deformation of net using the lumped mass method, and studied the effect of flexible net on steady flow field. All of these studies were concerned with the case of currents without accounting the wave effects. Tang et al. (2011) concentrated on the dynamic properties of a dual pontoon floating structure with an attached fish ignoring deformation based on the 2D potential theory and MEL technique.

In the present study, we applied a 3-D time-domain model based on the potential flow theory with nonlinear boundary conditions to investigate the hydrodynamic performance of the dual module system subjected wave action. A wave-maker based on an inner-source was adopt to generate input regular waves, with a starting rump function applied in order to eliminate the effect of transient disturbances. Thus, the reflection from the structure can pass through the source surface and be absorbed in a damping-layer behind. This inner-domain source technique has been employed in many fields, such as Ning et al. (2008, 2015), Wei et al. (1999) and Hafsia et al. (2009). However, so far, only few studies have been done on wave interaction with a pontoon-net floating breakwater in cases of typically occurring long waves by using the wave generation approach. The effects of flexible nets on wave scattering by the floating breakwater were simulated by means of a porous media model. The adaptation of a convenient mesh regridding and interpolation is performed to allow arbitrary body and free surface motions. In order to validate our numerical model, we confirmed the hydrodynamic performances obtained from numerical solutions with a series of on-site tests, which were conducted in South China sea.

The present paper is organized as follows. In Section 2, a mathematical model for the dynamics of the pontoon-net FB system in waves is presented based on the nonlinear boundary conditions. In Section 3, the prototype configuration and the comparisons between the numerical results and measured data from on-site tests are described in detail. Section 4 presents and discusses the hydrodynamic properties of the dual module system with different design parameters i.e. wave height, wave period, wave amplitude, net height and net porosities. Lastly, the conclusions of this study are given in Section 5.

2. Numerical model

2.1 Governing equation and boundary conditions

When the waves interact with the FB system as shown in Fig. 1, the numerical analysis are conducted in a numerical wave tank (NWT). In this model, two right-hand Cartesian coordinate systems are respectively defined. One is a space-fixed coordinate system $o_0x_0y_0z_0$ with the plane $o_0x_0y_0$ in the undisturbed free surface and the z_0-axis pointing vertically upwards. The other is a body-fixed coordinate system $o'x'y'z'$ with its origin o' placed at the mass center of the floating body. When the FB is at its equilibrium position, the two sets of coordinate systems are parallel to each other. Here, $\boldsymbol{\zeta}=(\zeta_1, \zeta_2, \zeta_3, \zeta_4, \zeta_5, \zeta_6)$ is defined to denote the surge, the sway, the heave, the pitch, the roll and the yaw, respectively. According to the assumption of incompressible, inviscid and irrotational fluid flow, the velocity potential Φ satisfies the Poisson equation in the fluid domain Ω

$$\nabla^2\Phi=q^* \tag{1}$$

where $q^*=2v\delta(x-x_s)$ denotes the pulsating volume flux density of the internal source, x_s=horizontal coordinate of wave source, v=horizontal wave velocity and $\delta(x-x_s)$ is the Dirac delta function. In this study, the horizontal wave velocity can be obtained by using the fifth-order Stokes wave theory (Fenton, 1985):

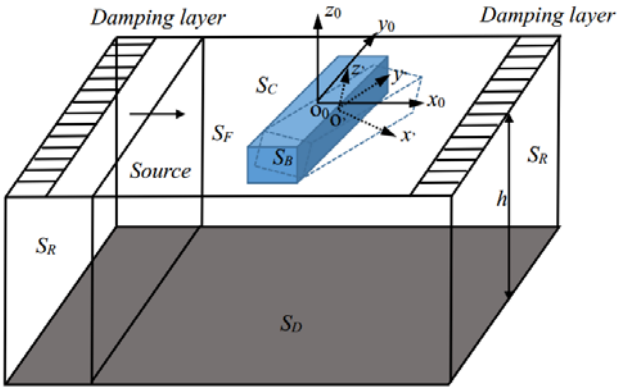

Fig. 1. Schematic diagram of waves interaction with a FB

$$\Phi_1 = \frac{\omega}{k^2}\sum_{i=1}^{5}\delta_i \cosh(ik(z+d))\cdot\sin(i\theta) \tag{2}$$

$$\eta_1 = \frac{1}{k}\sum_{i=1}^{5}\varepsilon_i \cos(i\theta) \tag{3}$$

$$\theta = kx - \omega t + \theta_0 \tag{4}$$

$$\begin{cases} \delta_1 = \kappa A_{11} + \kappa^3 A_{13} + \kappa^5 A_{15} \\ \delta_2 = \kappa^2 A_{22} + \kappa^4 A_{24} \\ \delta_3 = \kappa^3 A_{33} + \kappa^5 A_{35} \\ \delta_4 = \kappa^4 A_{44} \\ \delta_5 = \kappa^5 A_{55} \end{cases} \tag{5}$$

$$\begin{cases} \varepsilon_1 = \kappa \\ \varepsilon_2 = \kappa^2 B_{22} + \kappa^4 B_{24} \\ \varepsilon_3 = \kappa^3 B_{33} + \kappa^5 B_{35} \\ \varepsilon_4 = \kappa^4 B_{44} \\ \varepsilon_5 = \kappa^5 B_{55} \end{cases} \tag{6}$$

where ω, k, θ_0 and d denote wave frequency, wave number, initial phase and water depth, respectively; A_{ij}, $B_{ij(i,\,j=1\sim5)}$ and κ are the coefficients and have been given by Fenton (1985).

The time-dependent nodes on the instantaneous free water surface S_F are updated using the mixed Eulerian-Lagrangian (MEL) method in this paper. To gradually absorb the scattering waves at the both ends, two numerical damping layers with coefficient $\upsilon(r)$ are added in water surface conditions. Thus, free surface condition can be given in the Lagrangian form:

$$\begin{cases} \dfrac{d(x,y,\eta)}{dt} = \nabla\Phi - \nu(x)((x,y,\eta)-(x_0,y_0,0)) \\ \dfrac{d\Phi}{dt} = \dfrac{1}{2}\left|\nabla\Phi\right|^2 - g\eta - \nu(x)\Phi \end{cases} \tag{7}$$

where d/dt is the material derivative defined by $d/dt = \partial/\partial t + \nabla\Phi \cdot \nabla$. η denotes the free surface elevation. The damping coefficient $v(r)$ can be given

$$v(x) = \begin{cases} \alpha_d \omega \left[\dfrac{x - x_{1(2)}}{1.5\lambda} \right]^2, & x \geq x_1 \ \ or \ \ x \leq x_2 \\ 0, & otherwise \end{cases} \tag{8}$$

where $x_{1(2)}$ is the starting positions of damping layer, ω is the wave frequency, and α_d is the damping coefficient, λ is incident wavelength.

The boundary conditions on the seabed S_D and the side surface S_C are impermeable. And the boundary condition on instantaneous body surface S_B can be written as

$$\frac{\partial \Phi}{\partial n} = \left[(\dot{\zeta}_1, \dot{\zeta}_2, \dot{\zeta}_3) + (\dot{\zeta}_4, \dot{\zeta}_5, \dot{\zeta}_6) \times \mathbf{r} \right] \cdot \mathbf{n} \tag{9}$$

where $\boldsymbol{n}=(n_x, n_y, n_z)$ is the unit normal vector of the body surface pointing out of the fluid domain, $\mathbf{r}$ is the position vector in the body-fixed coordinate system.

The net boundary condition from the Darcy's law (the linear relation between the pressure drop and velocity) can be expressed

$$\frac{\partial \varphi}{\partial n} = \left[(\dot{\zeta}_1, \dot{\zeta}_2, \dot{\zeta}_3) + (\dot{\zeta}_4, \dot{\zeta}_5, \dot{\zeta}_6) \times \mathbf{r} \right] \cdot \mathbf{n} + \frac{\sigma}{\omega} \left(\frac{\partial \varphi^+}{\partial t} - \frac{\partial \varphi^-}{\partial t} \right), \ \text{on} \ S_S \tag{10}$$

where the superscripts mean $x_c \pm 0$, and x_c denotes the x coordinate of the nets. σ denotes the viscous effects called as the linear porous resistance and has been defined by Ji et al. (2018) according the corresponding experimental data.

2.2 Numerical solution

Green's identity is used to converted the above boundary value problem for Φ into an integral equation over its closed boundary

$$\chi(p_s)\phi(p_s) = \iint_L G(p_s, q_f) \frac{\partial \Phi(q_f)}{\partial n} - \phi(q_f) \frac{\partial G(p_s, q_f)}{\partial n} ds \tag{11}$$

where L denotes the whole boundary surface including S_F, S_B, S_D, S_S and S_C; solid angle coefficient χ has been given in Ning et al. (2015); $p_s=(x_s, y_s, z_s)$ and $q_f=(x_f, y_f, z_f)$ denote source point and field point, respectively; G is the Green function. In this paper, both the fluid domain and the shape of the FB are symmetric about the plane with y=0, and the water depth is constant. Thus, the Green function in this study is based on a simple Rankine source and its image with respect to symmetry plane and seabed:

$$G(p_s, q_f) = -\frac{1}{4\pi} \sum_{i=1}^{4} \frac{1}{r_i} \tag{14}$$

where

$$\begin{cases} r_1 = \sqrt{(x_f - x_s)^2 + (y_f - y_s)^2 + (z_f - z_s)^2} \\ r_2 = \sqrt{(x_f - x_s)^2 + (y_f + y_s)^2 + (z_f - z_s)^2} \\ r_3 = \sqrt{(x_f - x_s)^2 + (y_f - y_s)^2 + (z_f + z_s + 2d)^2} \\ r_4 = \sqrt{(x_f - x_s)^2 + (y_f + y_s)^2 + (z_f + z_s + 2d)^2} \end{cases} \tag{15}$$

Then, the remaining curved boundaries are discretized using a series of eight-node quadratic isoparametric elements. Within each element, physical parameters i.e velocity potential and space coordinates are interpolated by using a quadratic shape functions $h_i(\xi, \eta)$. Finally, the entire integral equation can be assembled into the following matrix form

$$[A]\{\boldsymbol{x}\}=\{B\} \tag{16}$$

where $\boldsymbol{x}$ includes the normal derivative of the potential on free surface and the potential on solid surface, and influence coefficient matrix [**A**] and vector {**B**} can be obtained from Eq. (11).

Once Eq. (16) is solved, the time series of wave evaluation at any location can be obtained, and the transmission, reflection and energy loss coefficients can be given

$$C_t=\frac{A_t}{A_i},\ C_r=\frac{A_r}{A_i},\ C_l=1-C_t^2-C_r^2 \tag{17}$$

where C_t, C_r and C_l denote the transmission, reflection and energy loss coefficients, respectively. The amplitudes of the incident wave (A_i) and the reflected wave (A_r) are separated by two-point method (Goda and Suzuki, 1976), and the amplitude of transmitted wave (A_t) is measured using the wave gauges installed downstream from breakwater

2.3 Hydrodynamic force and body motion

The motion equation of FB system can be written as

$$[M]\boldsymbol{\zeta}=\mathbf{F_h}+\mathbf{F_e} \tag{18}$$

Where matrix [M] includes the mass and rotational inertia; $\mathbf{F_e}$ is the external force or moment, i.e. the mooring force which is calculated using a special global coordinate-based finite element method (FEM) and the detail can be found in Cheng et al. (2018); $\mathbf{F_h}(f_1, f_2, f_3, f_4, f_5, f_6)$ is the hydrodynamic force or moment which can be obtained:

$$f_i=-\rho\iint_{S_B}(\Phi_t+\frac{1}{2}|\nabla\Phi|^2+gz)n_i dS \tag{19}$$

where ρ is the fluid density. The last two terms can be straightforwardly calculated, while the first term Φ_t is not clearly known. Therefore, some auxiliary functions (Wu and Eatock Taylor, 2003) which satisfy the Poisson equation in the fluid domain are introduced. These functions on free surface are zero and their normal derivatives are equal to the unit normal component of the body. Based on Green's identify, the results of auxiliary functions ψ_i (i=1, 2, 3, 4, 5, 6) can be achieved using similar solution with above potential velocity, and then the motion equation can be obtained

$$\sum_{j=1}^{6}(m_{ij}+c_{ij})\frac{d^2\zeta_j}{dt^2}=V_i-m_{33}g\delta_{i3}+f_{ei} \tag{22}$$

where

$$c_{ij}=\iint_{S_B}\rho\psi_i n_j dS \tag{23}$$

$$V=\rho\iint_{S_B}\begin{bmatrix}\nabla\psi_i\left[\left[(\dot{\zeta}_1,\dot{\zeta}_2,\dot{\zeta}_3)+(\dot{\zeta}_4,\dot{\zeta}_5,\dot{\zeta}_6)\times\mathbf{r}\right]\cdot\mathbf{n}\right]\cdot\left[\nabla\Phi-\left[(\dot{\zeta}_1,\dot{\zeta}_2,\dot{\zeta}_3)+(\dot{\zeta}_4,\dot{\zeta}_5,\dot{\zeta}_6)\times\mathbf{r}\right]\right]+\\ \psi_i((\dot{\zeta}_4,\dot{\zeta}_5,\dot{\zeta}_6)\times(\dot{\zeta}_1,\dot{\zeta}_2,\dot{\zeta}_3))\cdot\mathbf{n}\end{bmatrix}dS \\ -\rho\iint_{S_B+S_F}\left[gz+\frac{1}{2}|\Phi|^2\right]\frac{\partial\psi_i}{\partial n}dS \tag{24}$$

where m_{ij} is the coefficients in mass matrix [M].

2.4 Mesh regridding

The free surface condition indicated in Eq. (7) reveals that the nodes on free surface move horizontally and vertically. Thus, the discrete nodes may cluster or scatter as time continues. When the whole computational boundary does not change obviously, mesh distribution on free surface is performed using the spring analogy method (Batina, 1990) to obtain the horizontal location of new nodes. The vertical location on free surface can be obtained using corresponding interpolation of shape function at nodes.

The mesh distribution on the body surface is resolved at each time by regenerating and transferring information from the old mesh to the new one. For example, when floating moves from initial time t_0 to next time $t_0+\Delta t$, the body motion can be transformed to the motion of the calm water surface. Then, a series of Cubic B-Spline functions based the accumulated chord length are used to divide the mesh of the body and the node location in the body-fixed system. Thus, the node coordinate in the body-fixed system can be transferred to that in the space-fixed system as follows:

$$\begin{Bmatrix}x\\y\\z\end{Bmatrix}=\begin{bmatrix}\cos\zeta_4\cos\zeta_5 & \cos\zeta_4\sin\zeta_6+\sin\zeta_4\sin\zeta_5\cos\zeta_6 & \sin\zeta_4\sin\zeta_6-\cos\zeta_4\sin\zeta_5\cos\zeta_6\\ -\cos\zeta_4\sin\zeta_5 & \cos\zeta_4\cos\zeta_6-\sin\zeta_4\sin\zeta_5\sin\zeta_6 & \sin\zeta_4\cos\zeta_6+\cos\zeta_4\sin\zeta_5\sin\zeta_6\\ \sin\zeta_5 & -\sin\zeta_4\cos\zeta_5 & \cos\zeta_4\cos\zeta_5\end{bmatrix}^{-1}\begin{Bmatrix}x'\\y'\\z'\end{Bmatrix}+\\ \begin{Bmatrix}\zeta_1+x_G\\\zeta_2+y_G\\\zeta_3+z_G\end{Bmatrix} \tag{25}$$

All motion boundary surfaces can be re-gridded and updated at each time step. Based on the coordinates of new nodes, the integral equation over whole new boundary can be solved. Above mesh division can ensure constant number of elements by maintaining the number of half-cross profile. The size of meshes can also be controlled by making use of the given longitudinal and transverse element number or the given ratio of element length to element width.

3. Model validation

3.1 Prototype configuration

The cylindrical dual pontoon-net FB (as shown in Fig. 2a) combines the advantages and design features of dual pontoon structure and flexible nets. The attractive merits of this FB include high wave attenuation capacity, favorable motion performance, low construction cost and environmental friendliness. Then, the dual-module FB system with total length 33m (as shown in Fig. 2b) was manufactured as the test model and moored at the site 370m away from the tested platform. The test model has two modules connected by an elastic rubber connector with the length of 3 m. Each module has the length 15 m× breadth 20 m, consisting of two 8 m (diameter)×15 m (length) cylinders which is attached with four rows of plane nets underneath at intervals of 3 m (Wu et al., 2020). The plane net is made of knotless polythylene (PE) with solidity ratio 0.3, submerged height 8 m, length 15 m. To measure the wave elevation and obtain the wave attenuating capacity, two ADCPs are placed from the front and the rear of the FB system, respectively.

(a) Single-module design (b) Dual-module system

Fig. 2. Cylindrical dual pontoon floating breakwater (Wu et al., 2020)

3.2 Comparison

To verify the accuracy of the present numerical method, the hydrodynamic performance of the FB system subjected to wave load with various wave period is considered. Fig. 3 shows the comparison of the predicted and the measured results of the transmission coefficients which are obtained by regarding the average value of the significant wave heights as the characteristic wave height. To examine the wave attenuating capacity of the FB system, the target values of C_t for different wave periods are defined according the design requirement of wave energy elimination from open sea and are also shown in the figure. In all the cases, the correlation between the predicted and measured values is reasonable. The numerical model overestimates the practical measured attenuating effect for 10% to 23% within the whole tested range of wave periods, which can be attributed to the possibly un-captured physics (such as turbulence) and inherent nonlinearity in the viscous effects. Both in the prediction and measurement, it is seen that the transmission coefficient increases with the wave period, and are smaller than the assigned target values, which further verifies the successful design of the breakwater.

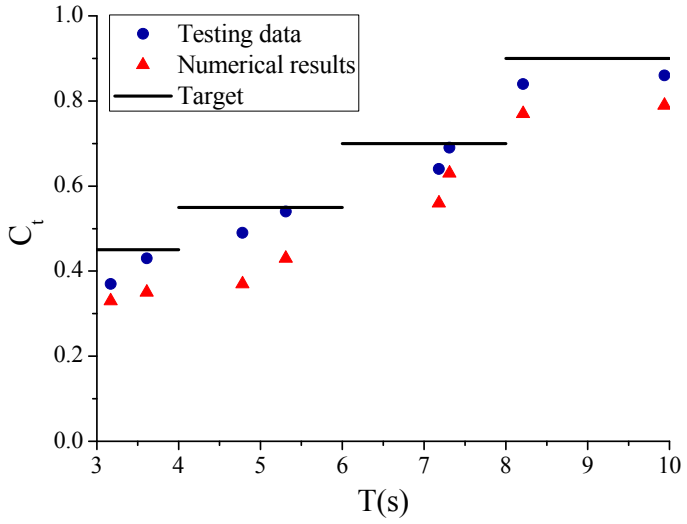

Fig. 3. Comparison of the predicted and the measured results

4. Parametrical studies

4.1 *Net number*

In general, the reflection coefficient C_r, the transmission coefficient C_t, the energy loss coefficients C_l, and the response amplitude operators (RAOs) are used to describe the hydrodynamic performance of the floating breakwater. Therefore, the sway, heave and roll RAOs are defined as

sway RAO= A_{sway}/A_I, heave RAO= A_{heave}/A_I and roll RAO= A_{roll}/A_I, respectively, where A_{sway}, A_{heave}, and A_{roll} are defined as the first-order oscillation amplitudes relative to the mean position of the floating breakwaters in waves. The influences of the net numbers on the structure's dynamic properties are shown in Figs.4 and 5. In these figures, the lines represent the numerical solutions, whereas the symbols stand for the experimental data.

Fig. 4 shows the variation of the reflection, transmission and energy loss coefficients with dimensionless wave frequency $g/(\omega^2 h)$ for four different conditions (i.e., without net, one row net, two row nets, and three row nets) at incident amplitude A_I=1.3 m, submerged net depth d_{net}=8 m and solidity ratio S=0.4. It can be observed that the reflection, transmission and energy loss coefficients for different net numbers exhibit the same trend, but the maximum or minimum values correspond to lower wave frequencies with increasing the number of the plane net. This is mainly caused by an increased added mass and damping effect between fluid-net interaction. When the FB has net, the reflection coefficient in the high frequency region, $g/(\omega^2 h)$<0.4, is slightly larger than its counterpart, which is because the net cage increases the seaward area of the whole structural system, resulting in an increased reflection; however, this opposite is true for the case of two and three rows of net, which is due to the energy dissipation induced by the fluid-net interaction. The sudden drop of transmission coefficients occurs at $g/(\omega^2 h)$=0.6~0.8 and 1.2~1.4, which corresponds to the resonant motions of floating breakwaters. Also, the energy loss coefficients show the peak values at the resonant periods. This indicates that when the incident wave period is close to the natural period of floating breakwaters, the wave energy is transformed into the kinetic energy of the structure, and the transmitted wave energy will be reduced by the same condition and vice versa for dissipated energy, resulting in a sudden variation transmission or energy loss coefficient. Moreover, the bandwidth of maintaining high energy loss coefficients are gradually broadened with the net number.

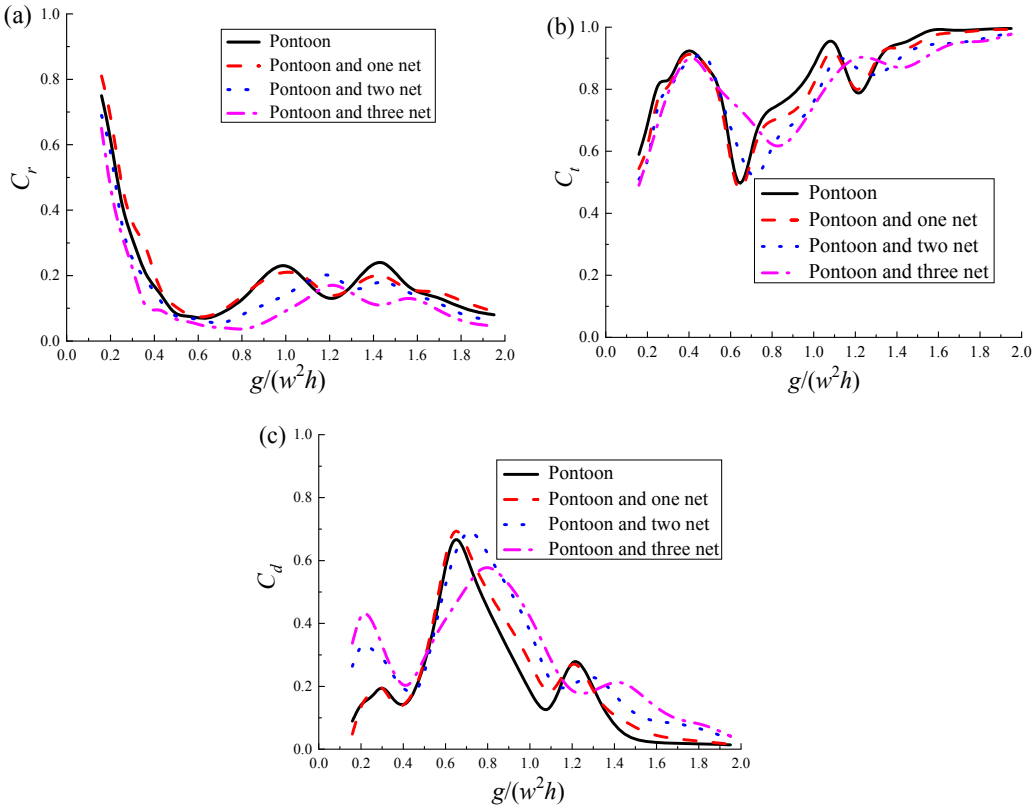

Fig. 4. Comparisons of the numerical and experimental results as a function of dimensionless wave frequency $g/(\omega^2 h)$ and net number. (a) Reflection, (b) transmission coefficient, and (c) energy loss coefficient

Fig. 5 numerically shows the changes in the sway, heave and roll RAO of the dual pontoon floating breakwater with and without vertical nets underneath versus dimensionless wave frequency $g/(\omega^2 h)$ for the following fixed parameters: A_i=1.3 m, d_{net} =8 m, and S=0.4. It can be observed that an increase of net number results in a slight larger sway motion in high frequency region ($g/(\omega^2 h)$<0.6) and vice versa in low frequency region ($g/(\omega^2 h)$>0.6). This characteristic indicates that for long waves, the viscous dissipated energy induced by the net can effectively reduce the sway motion. In addition, the heave and roll motion performances are more favorable when increasing net number from one to three rows, which is due to the damping effect of fluid-net interaction and moment of inertia. The heave and roll motion have peak values at $g/(\omega^2 h)$=0.6 ~0.8 and 1.2~1.4, respectively, corresponding to the natural frequencies. On the other hand, the peak values of the heave and roll motions move to lower frequency region with increasing net number, but the trends of motion responses versus the wave frequency for all cases are similar. It is also confirmed that the wave frequency values $g/(\omega^2 h)$=0.6 ~0.8 and 1.2~1.4, where the resonant motions of heave and roll occur, correspond to turning point positions of the transmission and energy loss coefficients shown in Fig.4. The wave attenuating effect of the FB with and without nets is more closely dependent to the heave motion than roll motion, especially at the resonant frequency. The numerical solutions show good agreement with the measured data.

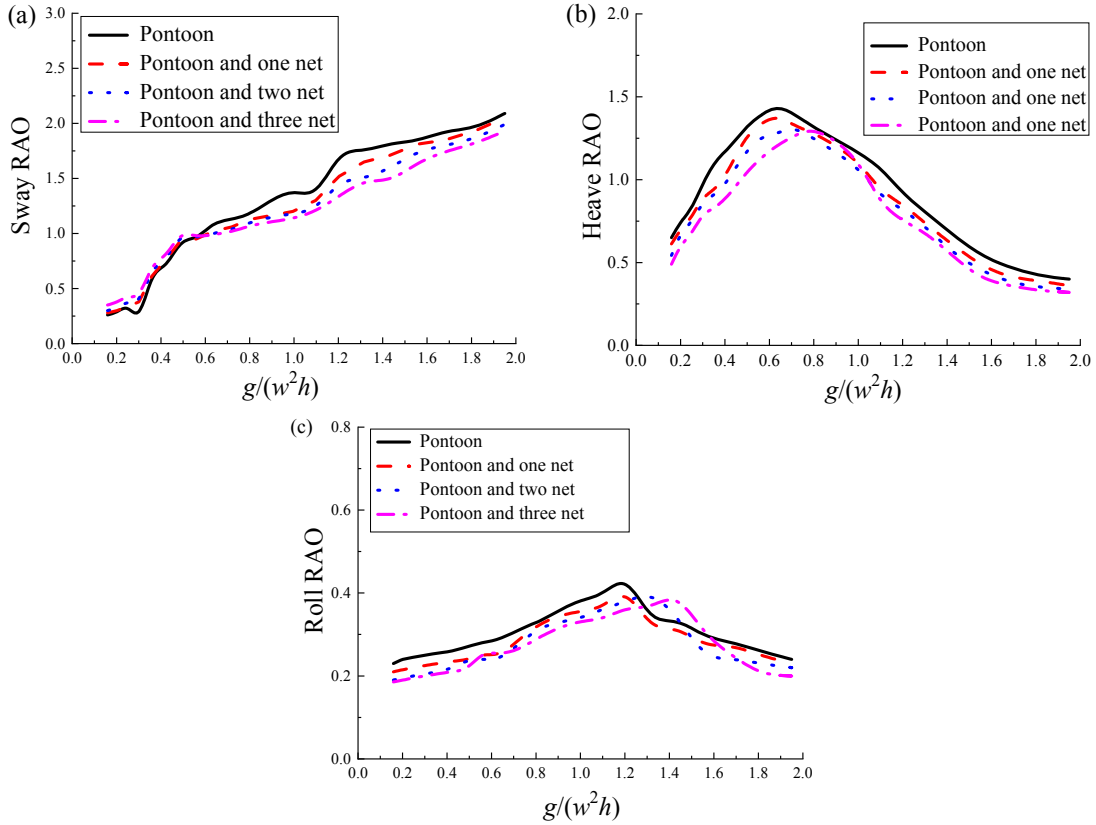

Fig. 5. Variations of (a) sway RAO, (b) heave RAO and (c) roll RAO versus dimensionless wave frequency $g/(\omega^2 h)$ and net number

4.2 *Net depth*

All aforementioned numerical solutions are given for a fixed net depth, d_{net}. To further examine the

sensitivity of net depth, additional numerical simulations of d_{net}=6 m and 10 m are also carried out and plotted in Figs. 6-7 for the following fixed net parameters: three rows of net, A_i=1.3 m, and S=0.4. Fig. 6a-c shows the reflection, transmission and energy loss coefficients as a function of the dimensionless wave frequency $g/(\omega^2 h)$ and net height d_{net}/h. These coefficients for different net depths exhibit the same trend, but as the net height increases, the reflection and transmission coefficients are reduced for a wide range of wave frequency and vice versa for the energy loss coefficient, which means that the deeper nets more effectively interact with waves to more wave energy dissipation. Moreover, the minimum reflection and transmission coefficients and the maximum energy loss coefficient for different net heights correspond to almost the same wave frequency, close to 0.8 and 1.4. This suggests that the net height has weak influence on the occurring condition of the minimum reflection and transmission coefficients and maximum energy loss coefficient but affects their magnitudes.

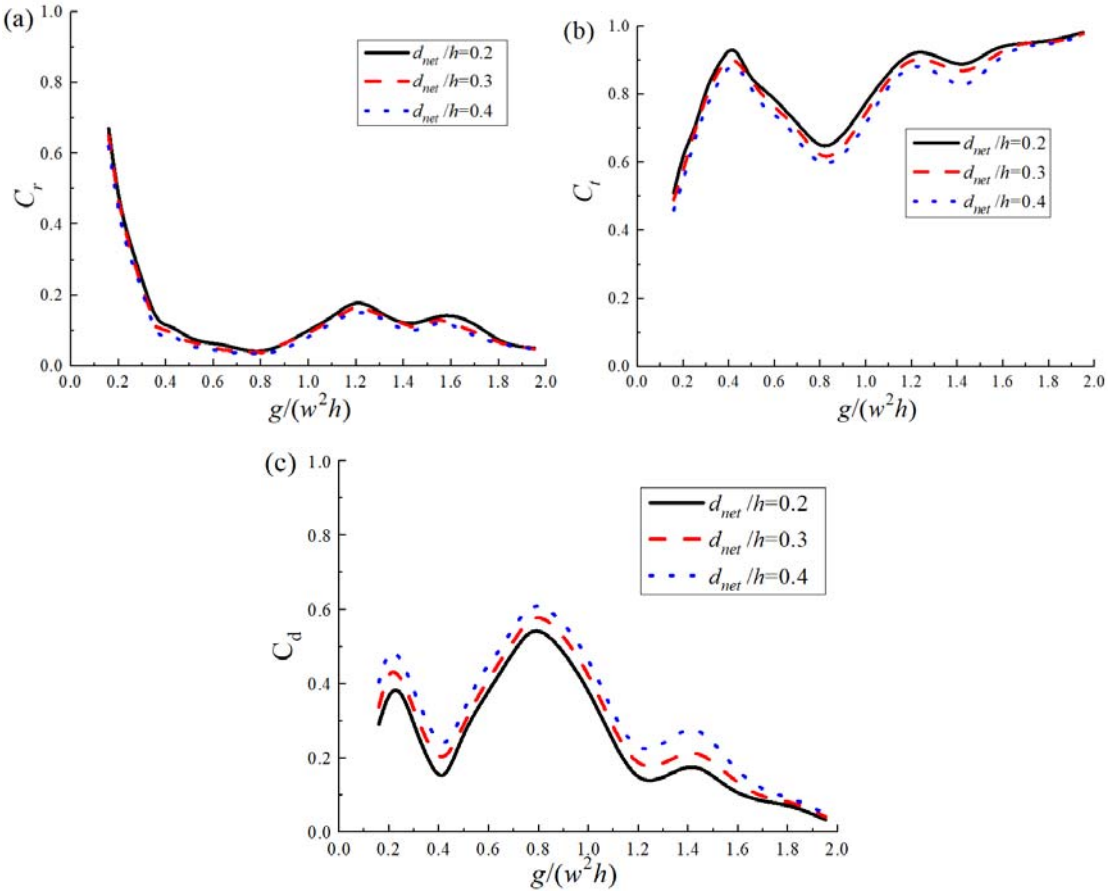

Fig. 6. Comparisons of the numerical and experimental results as a function of dimensionless wave frequency $g/(\omega^2 h)$ and net height d_{net}/h. (a) reflection, (b) transmission coefficient, and (c) energy loss coefficient

Fig. 7a-c gives the variation of the motion RAO of the FB with wave frequency $g/(\omega^2 h)$ and net height d_{net}/h. It reveals that the sway motion of the floating breakwater slightly increases with increasing the net depth in high frequency region $g/(\omega^2 h)$<0.6, but becomes slightly advantageous when $g/(\omega^2 h)$>0.6. This phenomenon can be explained from two factors: the seaward area and viscous energy dissipation of the net. Both the two parameters increase with net depth. However, the sway motion of the floating breakwater is inversely proportional to the viscous energy dissipation of the net, and is proportional to the seaward area due to the increase of wave force in the direction normal to the breakwater if the masses of the floating breakwater are the same. For

short waves, the effect of the seaward area on sway motion increases faster than that of the viscous energy dissipation as the net depth increases, and this opposite is true for long waves. Overall, the sway motion in this case are not very sensitive to the change of net depth. The deeper the net, the lower the resonant response of heave RAO, which may be because of the damping effect of the net. It is interesting that the roll motion is magnified when the net depth increases from d_{net}/h=0.2 to 0.3, but after that point d_{net}/h=0.3, the performance of the roll motion is improved with the increase of d_{net}/h. This example typically implies that the optimal design with net depth should be determined with rigorous analysis. Compared to the numerical results of the FB without nets in Section 4.2, Fig. 7c, the presence of vertical rows of net can provide a better reduction of the motion responses of the floating breakwater.

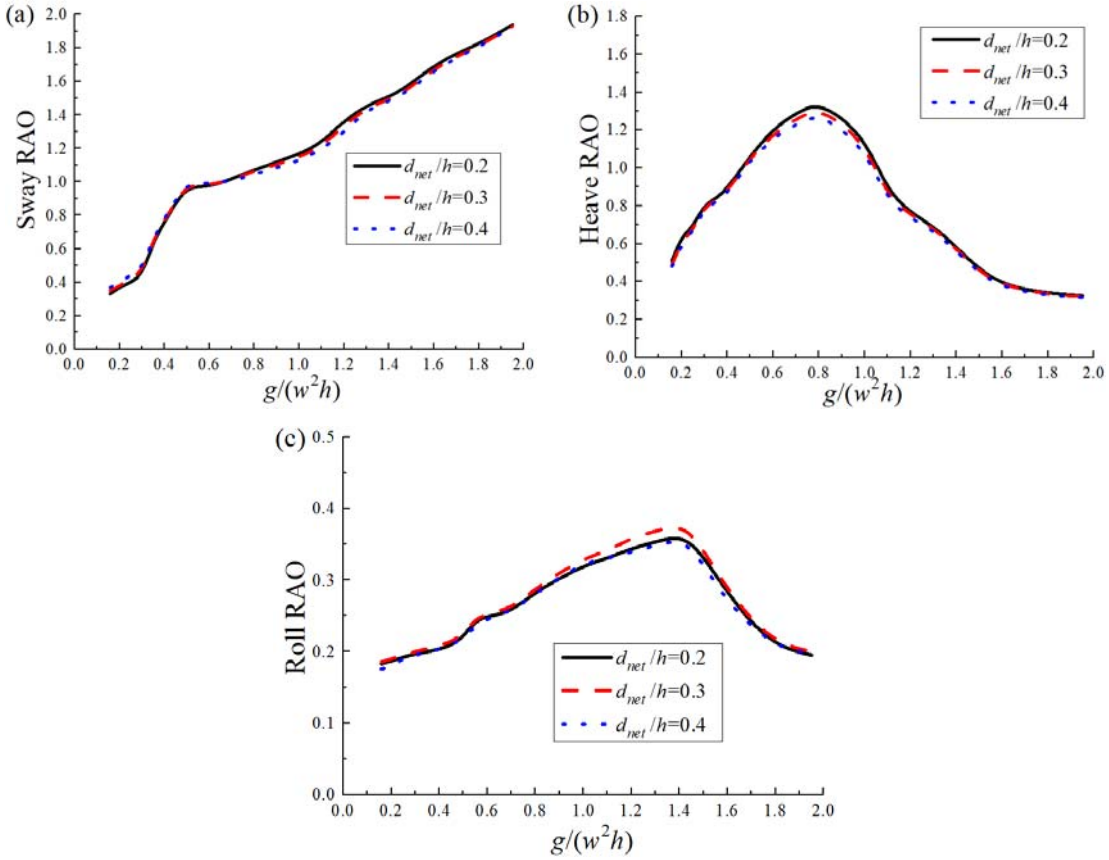

Fig. 7. Variations of (a) sway RAO, (b) heave RAO and (c) roll RAO versus dimensionless wave frequency $g/(\omega^2 h)$ and net height d_{net}/h

4.3 *Net solidity*

For the pontoon-net floating breakwater, the net solidity has an evident influence on the wave attenuation effectiveness of the floating breakwater. Fig. 8 shows the variations of the reflection, transmission and energy loss coefficients with the dimensionless wave frequency $g/(\omega^2 h)$ for varying values of net porosity when A_I=1.3 m, d_{net}=8 m and three rows of net while the rest of the input parameters are fixed using the given values. Compared to the numerical and experimental results of the FB without nets in Section 4.2, the wave energy dissipation effectiveness at S=0.15 of the DPFB with three rows of net has no obvious improvement. This may be because the porosity of the net at S=0.15 is quite large, which tends to approach transparent. However, the wave attenuating effect of the FB increases more significantly as the net solidity increases from S=0.15 to 0.4, which is due to the shielding effect and viscous damping effect of net. On the other hand, these coefficients

exhibit an oscillation with the variation of wave frequency. The minimum transmission coefficient and the maximum energy loss coefficient in the vicinity of $g/(\omega^2 h)$=0.6~0.8 and 1.2~1.4 increase and decrease with net solidity, respectively. This is because the maximum energy transfers from the waves to heave and roll motion of the floating structure decreases as the net solidity increases. That is, vertical rows of net with appropriate porosity can reduce the energy exchange between the waves and motion of the floating structure. The wave frequency for the minimum reflection and transmission coefficients and maximum energy loss coefficient vary with the net solidity, but the trends of the reflection, transmission and energy loss coefficients versus the wave frequency for S=0.15, 0.25 and 0.4 are similar. This feature is mainly due to the contribution from the fluid-net interaction.

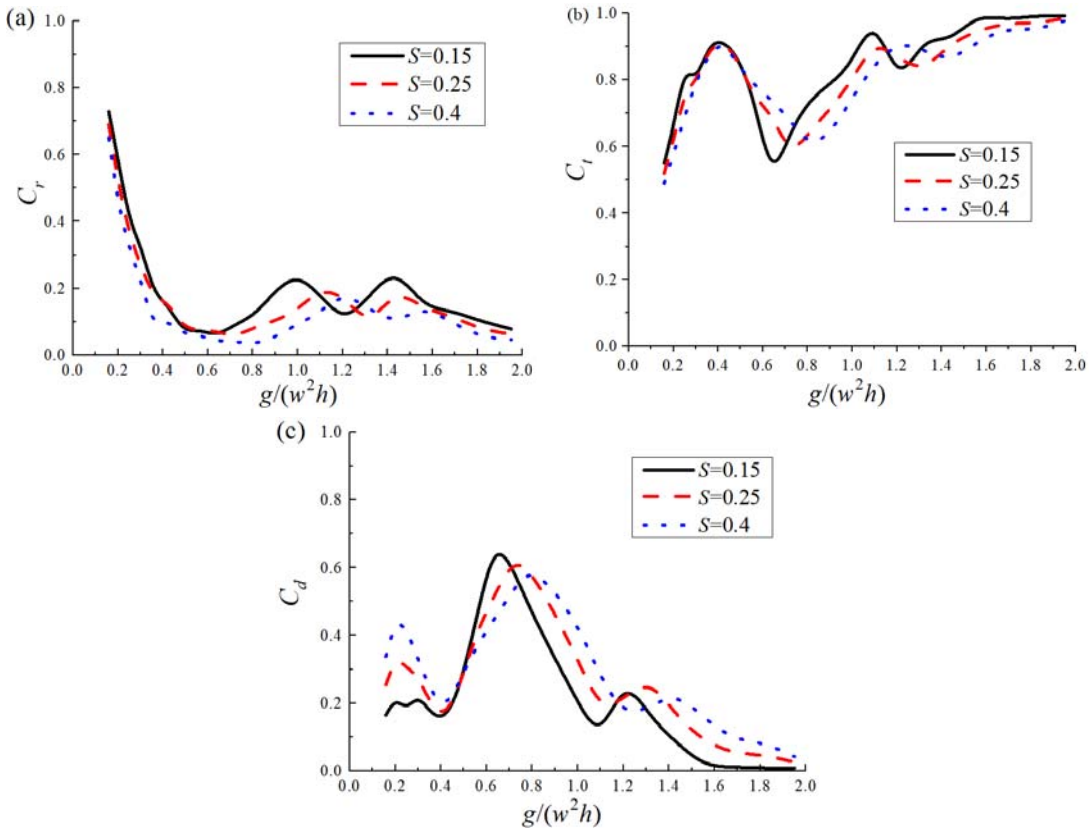

Fig. 8. Comparisons of the numerical and experimental results as a function of dimensionless wave frequency $g/(\omega^2 h)$ and net solidity S. (a) reflection, (b) transmission coefficient, and (c) energy loss coefficient

Fig. 9a-c shows the effects of the net solidity S on the sway, heave, and roll motions of the CDPNFB, respectively with A_I=1.3 m, d_{net}=8 m and three vertical rows of net. From Fig. 9(a), it can be observed that the sway motion of the floating breakwater decreases with increasing net solidity for long waves ($g/(\omega^2 h)$>0.6). This is because the incident waves are partly absorbed by the front two rows of net when waves propagate through the FB, while the rest of waves are transmitted through nets and onto the seaward surface of the rear pontoon, which leads to a reduction of wave forces on the rear pontoon. Fig. 9(b) indicates that the response of heave RAO becomes maximum in the vicinity of $g/(\omega^2 h)$=0.6, 0.7 and 0.8 for net solidity S=0.15, 0.25 and 0.4, respectively, which corresponds to the turning points of the reflection, transmission and energy loss coefficients (Fig. 7). This means that the resonant frequency gradually shifts down with the net solidity, and the positions of the minimum reflection and transmission coefficients and the maximum energy loss coefficient for various net solidities are near each resonant frequency. Also, the resonant response

of heave RAO becomes smaller as the net solidity increases. Fig. 9(c) reveals that the downshift of resonant frequency of Roll RAO is more significant than the decrease of maximum value when the net solidity increases.

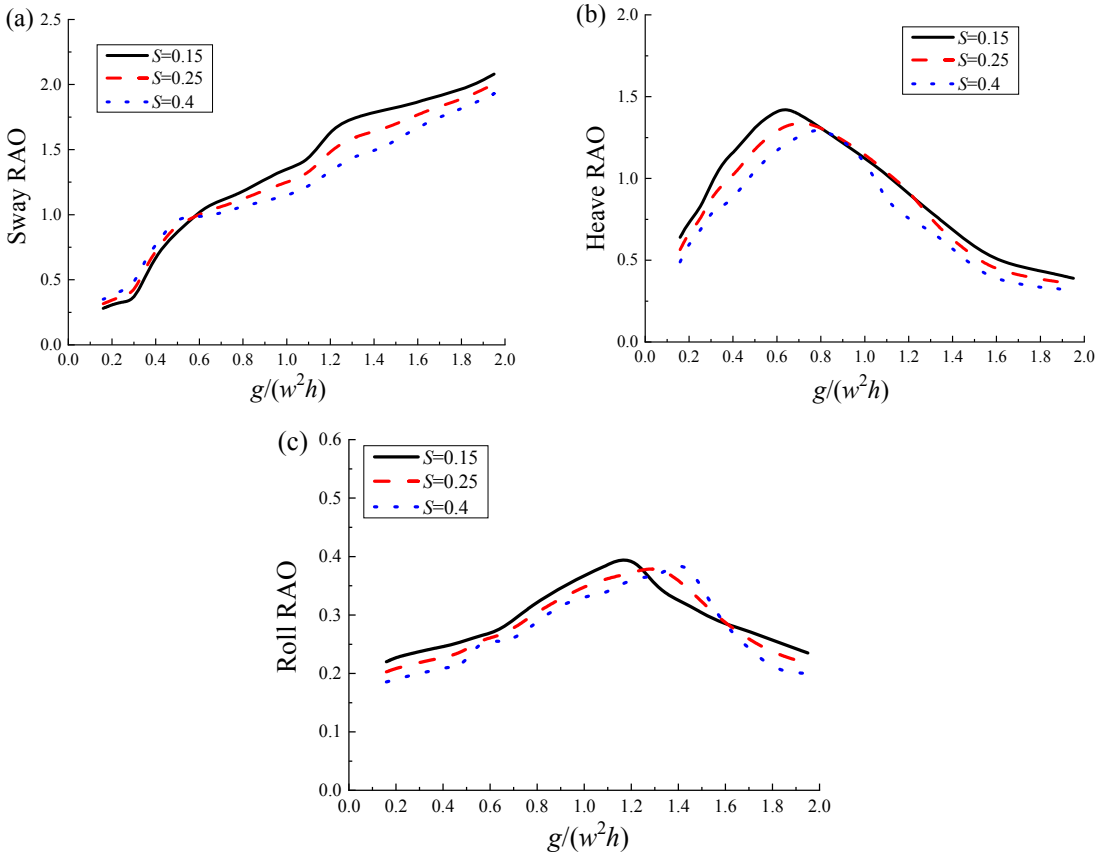

Fig. 9. Variations of (a) sway RAO, (b) heave RAO and (c) roll RAO versus dimensionless wave frequency $g/(\omega^2 h)$ and net solidity S

4.4 *Wave amplitude*

Finally, we consider the hydrodynamic performance of the CDPNFB with changes in the incident wave amplitude for d_{net}=8 m, S=0.4, and three vertical rows of net, as shown in Figs. 10-11. Fig. 10a-c shows the reflection, transmission and energy loss coefficients as a function of the dimensionless wave frequency $g/(\omega^2 h)$ and the incident wave amplitude A_I. The results reveal that the larger incident wave amplitude leads to the lower frequency position of the minimum reflection and transmission coefficients and the maximum energy loss coefficient. In addition, the minimum reflection and transmission coefficients at the vicinity of $g/(\omega^2 h)$=0.8~0.9 and 1.4~1.5 decreases with increasing incident wave amplitude, and vice versa for energy loss coefficient. This might include two factor: the energy dissipation induced by the fluid-net interaction and the energy transfer from waves to motion of the floating breakwater. However, the kinetic energy of the floating breakwater at resonant frequencies almost remain the same results among various wave amplitudes (see Fig. 10b-c). Therefore, when the structure is exposed to higher waves, the wider concentration range of the wave energy broadens the area of interaction between the moving water particles and the net, which boosts the wave attenuation effectiveness of the nets. This also indicates that for practical applications such as shoreline or marine structure protection, a dual pontoon with deeper protruding plane nets should be more advisable, since not only lower reflection and transmission can be achieved, but its application can also be extended to a wider range of wave lengths and wave

amplitudes.

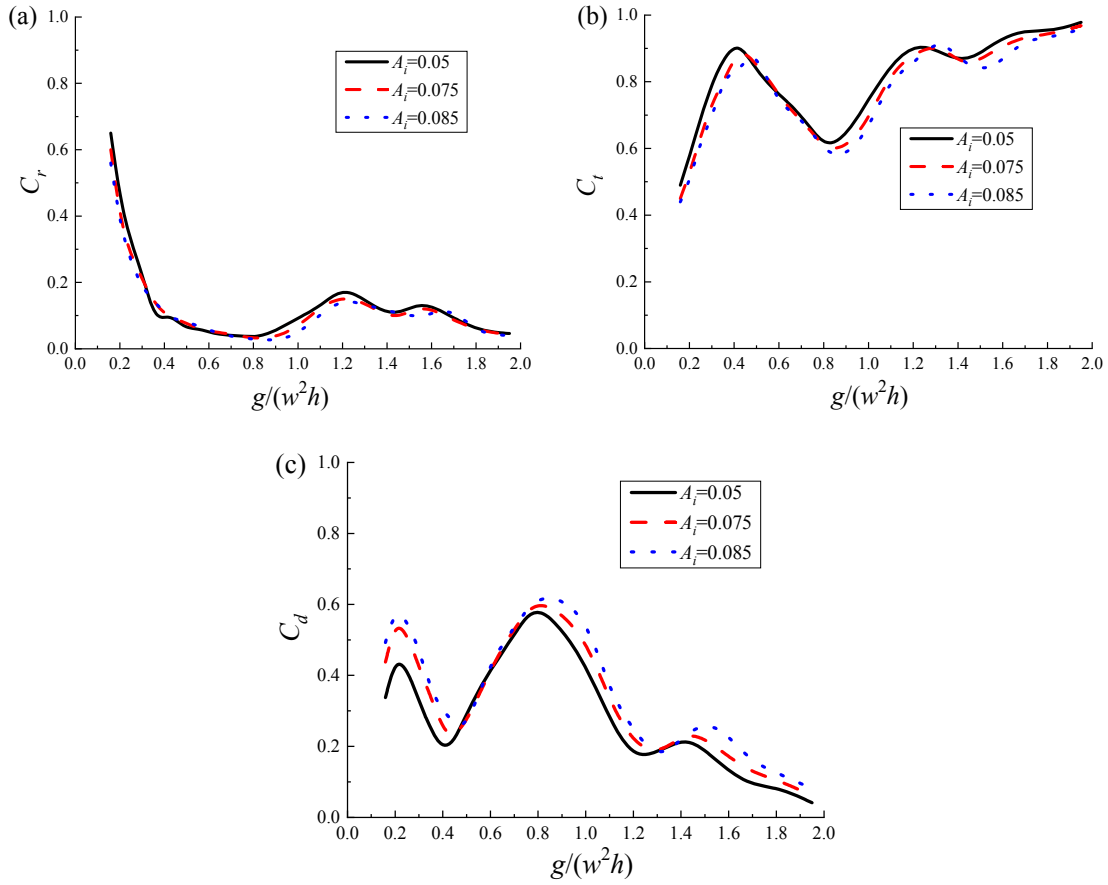

Fig. 10. Comparisons of the numerical and experimental results as a function of dimensionless wave frequency $g/(\omega^2 h)$ and incident amplitude A_I. (a) reflection, (b) transmission coefficient, and (c) energy loss coefficient

Fig. 11a-c shows the computed motion responses of RAO versus the dimensionless wave frequency $g/(\omega^2 h)$ and the incident wave amplitude A_I. It can be observed that the sway responses of RAO for three incident wave amplitude have almost the same results, and the changes of peak values of heavy and roll RAOs are negligible with incident wave amplitude. This means that our floating breakwater configuration performs satisfactorily when A_I is approximately larger than 0.05 m, 0.075 m and 0.085 m for prototype incident wave amplitudes of 1m, 1.5m, and 1.75 m, respectively. The resonant frequencies of heave and roll RAOs shift down as the incident wave amplitude increases, but the incident wave amplitude has weak influence on the trend of motion response with the variation in wave frequency. This also matches the observation that the added mass and damping effect induced by the fluid-net interaction increase as incident wave amplitude increases, which will reduce the resonant frequency of the motion responses.

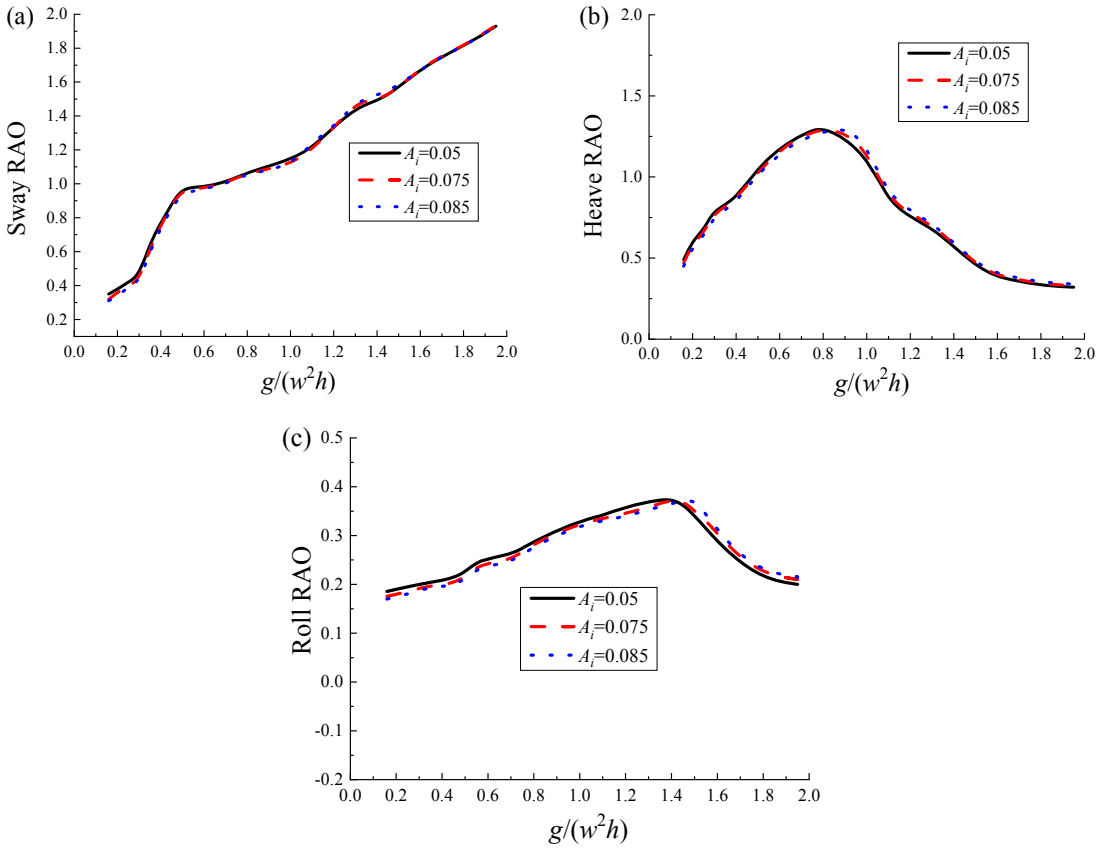

Fig. 11. Variations of (a) sway RAO, (b) heave RAO and (c) roll RAO versus dimensionless wave frequency $g/(\omega^2 h)$ and incident amplitude A_I

5. Conclusion

A numerical approach is proposed to simulate the interaction of waves and dual pontoon FB attached with one or more vertical nets based on the potential flow theory with fully nonlinear boundary conditions. In the numerical approach, an internal wave-maker with the internal source is applied to generate the incident waves, and thus re-reflection phenomena at the input boundary are avoided. A porous-media model by using Darcy's law is used to simulate the flow field around vertical rows of net. The HOBEM with mixed Eulerian-Lagrangian approach is applied to update the instantaneous water particle on free surface. The numerical solutions are found to agree well with on-site tested data.

Using the developed computer program, the hydrodynamic performance of the FB system is assessed for various designed parameters, such as net number, net height, net solidity, and wave conditions. According to the results, the energy loss coefficient is enhanced by suspending one or more vertical rows of net underneath and vice versa for the reflection and transmission coefficients, which is explained by the energy dissipation from fluid-net interaction. The minimum reflection and transmission occur at the resonant frequencies of heave and roll motions, at which the energy loss coefficient is the largest. In addition, more nets lead to lower resonant frequencies, which is due to the increase of added mass and damping. Occurrence of the minimum reflection and transmission and the maximum energy loss coefficient is independent to the net depth, but that shifts down by the net solidity and incident wave amplitude. The reflection and transmission coefficients decrease with net depth and vice versa for the energy loss coefficient. No significant improvement on sway motion can be achieved by increasing the net depth when the net depth is larger than 20% water

depth, but the heave and roll RAO peaks generally decrease with increasing net depth. At the resonant condition, the transmission and energy loss coefficients increase and decrease with net solidity, respectively, which is caused by the reduction of maximum energy exchange between the waves and motion of the floating breakwater.

For the given net parameters, the resonant frequencies decrease with incident wave amplitude, but the corresponding maximum responses of heave and roll RAOs almost remain the identical results. This means that the reduction of the reflection and transmission coefficients at near resonant frequencies with increasing incident wave amplitude is due to more wave attenuation effectiveness of nets, which further validates the feasibility of the FB.

Acknowledgment

The authors are grateful to the National Natural Science Foundation of China (Grant No. 52025112, 51861130358), the State Key Laboratory of Ocean Engineering, China (Shanghai Jiao Tong University) (Grant No. 1905) and the Newton Advanced Fellowships (Grant No. NAF\R1\180304) by the Royal Society for supporting this work.

References

Brorsen, M., Larsen, J., 1987. Source generation of nonlinear gravity waves with the boundary integral equation method. Coast Engineering 11, 93-113.

Bi, C.W., Zhao, Y.P., Dong, G.H., Xu, T.J., Gui, F.K., 2014. Numerical simulation of the interaction between flow and flexible nets. J Fluid Struct. 45, 180-201.

Choo, Y.I., Casarella, M.J., 1971. Hydrodynamic resistance of towed cables. Journal of Hydronautics 5(4), 126-131.

Cheng, Y., Ji, C.Y., Ma, Z., Zhai, G.J., Oleg, G., 2017. Numerical and experimental investigation of nonlinear focused waves-current interaction with a submerged plate. Ocean Eng. 135, 11-27.

Cheng Y., Ji, C. Y., Zhai, G. J., Oleg, G., 2018. Nonlinear analysis for ship-generated waves interaction with mooring line/riser systems. Mar Struct. 59, 1-24.

Chen, W.C., Dolguntseva, I., Savin, A., Zhang, Y.L., Li, W., Svensson, O., Leijion, M., 2017. Numerical modelling of a point-absorbing wave energy converter in irregular and extreme waves. Appl Ocean Res. 63, 90-105.

Fredriksson, D.W., 2001. Open ocean fish cage and mooring system dynamics. Ph.D. Dissertation, University of New Hampshire, Durham, NH, USA.

Fenton JD. A fifth order stokes theory for steady waves, J Waterw Port Coast. 1985;111:216-234.

Gerhard, K., 1983. Fibre Ropes for Fishing Gear. FAO Fishing Manuals. Fishing News Books Ltd., Farnham, UK81-124.

Goda, Y., Suzuki, Y., 1976. Estimation of incident and reflected waves in random wave experiments. In: Proceedings of the 15th Coastal Engineering Conference, Honolulu, Hawaii, pp. 828-845.

Hadzic, I., Hennig, J., Peric, M., Xing-Kaeding, Y., 2005. Computation of flow-induced motion of floating bodies. Applied Mathematical Modelling 29, 1196-1210.

Hafsia, Z., Haj, M.B., Lamloumi, H., Maalel, K., 2009. Comparison between moving paddle and mass source method for solitary wave generation and propagation over a steep sloping beach. Engineering Applications Computional Fluid Mechanics 3(3), 355-368.

Johansson, D., Juell, J.E., Oppedal, F., Stiansen, J.E., Ruohonen, K., 2007. The influence of the pycnocline and cage resistance on current flow, oxygen flux and swimming behaviour of Atlantic salmon (Salmo salar L) in production cages. Aquaculture 265(1), 271-287.

Ji CY, Cheng Y, Yang K, Oleg GD. Numerical and experimental investigation of hydrodynamic performance of a cylindrical dual pontoon-net floating breakwater. Coast Eng. 2017; 129: 1-16.

Koo, W.C., Kim, M.H., 2004. Freely floating-body simulation by a 2-D fully nonlinear numerical wave tank. Ocean

Eng. 31, 2011-2046.

Koo, W.C., Kim, M.H., 2007. Fully nonlinear wave-body interactions with surface-piercing bodies. Ocean Eng. 34, 1000-1012.

Kristiansen, T., Faltinsen, O.M., 2012. Modelling of current loads on aquaculture net cages. J Fluid Struct. 34(2012), 218-235.

Loland, G., 1991. Current force on flow through fish farms (Ph.D. dissertation). Norwegian Institute of Technology, Trondheim, Norway.

Mittal, S., Kumar, V., 2001. Flow-induced oscillations of two cylinders in tandem and staggered arrangements. J Fluid Struct. 15(5), 717-736.

Ning, D.Z., Shi, J., Zou, Q.P., Teng, B., 2015. Investigation of hydrodynamic performance of an OWC (oscillating water column) wave energy device using a fully nonlinear HOBEM (higher-order boundary element method). Energy 83, 177-188.

Ning, D.Z., Teng, B., Eatock Taylor, R., Zang, J., 2008. Numerical simulation of non-linear regular and focused waves in an infinite water-depth. Ocean Eng. 35, 887-899.

Pham, X.P., Varyani, K.S., 2005. Evaluation of green water loads on high-speed containership using CFD. Ocean Eng. 32, 571-585.

Simonsen, C.D., Otzen, J.F., Joncquez, S., Stern, F., 2013. EFD and CFD for KCS heaving and pitching in regular head waves. J Mar Sci Tech-Japan. 18(4), 435-459.

Sadat-Hosseini, H., Wu, P.C., Carrica, P.M., Kim, H., Toda, Y., Stern, F., 2013. CFD verification and validation of added resistance and motions of KVLCC2 with fixed and free surge in short and long head waves. Ocean Eng. 59, 240-273.

Tang, H.J., Huang, C.C., Chen, W.M., 2011. Dynamics of dual pontoon floating structure for cage aquaculture in a two-dimensional numerical wave tank. J Fluid Struct. 27, 918-936.

Wei, G., Kirby, G.T., Sinha, A., 1999. Generation of waves in Boussinesq models using a source function method. Coast Engineering 36, 271-299.

Wu, YS, Ding J, Gu XK, et al. The progress in the verification of key technologies for floating structures near islands and reefs. Proceedings of the Thirtieth International Ocean and Polar Engineering Conference, Shanghai, China, 2020.

Westphalen, J., Greaves, D.M., Williams, C.J.K., Hunt-Raby, A.C., Zang J., 2012. Focused waves and wave-structure interaction in a numerical wave tank. Ocean Eng. 45, 9-21.

Zang, J., Gibson, R., Taylor, P.H, Eatock Taylor, R., Swan, C., 2006. Second order wave diffraction around a fixed ship-shaped body in unidirectional steep waves. J. Offshore Mech. Arct. Eng. 128, 10.

Zhao, Y.P., Bi, C.W., Dong, G.H., Gui, F.K., Cui, Y., Guan, C.T., X, T.J., 2013. Numerical simulation of the flow around fishing plane nets using the porous media model. Ocean Eng. 62, 25-37.